The International Journal of Advanced Manufacturing Technology (2024) 130:2799–2809
https://doi.org/10.1007/s00170-023-12841-9

ORIGINAL ARTICLE

Investigation of the influence of the AWJ-specific energy on the cutting kerf profile on aluminium 6082

Francesco Perotti[1,2] · Michele Monno[1] · Massimiliano Annoni[1]

Received: 4 August 2023 / Accepted: 6 December 2023 / Published online: 21 December 2023

Abstract
This study introduces the abrasive waterjet specific energy as a novel physical quantity to characterize the taper ratio in abrasive waterjet cutting. Said quantity was defined as a proper combination of the most influential control factors. A series of abrasive waterjet cutting experiments on aluminium 6082, were conducted, according to the design of experiments methodology. For each experimental run, the width of the kerf profile was measured and characterized in terms of taper ratio. The effect of the abrasive waterjet specific energy and the main process parameters on the measured quantities were investigated. Results showed that inside the experimental range of the process parameters, the abrasive waterjet specific energy correlates well with the taper ratio. As a conclusion, different combinations of the control factors (water pressure, abrasive mass flow rate, feed rate), corresponding to the same level of abrasive waterjet specific energy, produced the same cutting kerf geometry as well as the same taper ratio. This result gives freedom to the waterjet users in selecting the best parameter combination according to some criteria (e.g., time or cost) for achieving the target AWJ-specific energy and the consequent kerf quality.

Keywords Abrasive waterjet cutting · Specific energy · Kerf profile, Cutting quality

Abbreviations

p MPa	Water pressure
d_n mm	Primary orifice diameter
ρ kg•m^{-3}	Water density
v_{th} m•s^{-1}	Waterjet theoretical velocity
n, L -, MPa	Constants
v_j m•s^{-1}	Real jet velocity
ψ -	Compressibility coefficient
c_v -	Velocity coefficient
c_d -	Discharge coefficient
$\dot{m}_w$ kg•s^{-1}	Water mass flow rate
Q_w m^3•s^{-1}	Water volume flow rate
S_n mm^2	Nominal cross-sectional area of the orifice
P_{hydr} W	Jet hydraulic power
$\dot{m}_a$ kg•min^{-1}	Abrasive mass flow rate
d_f mm	Focuser tube diameter
sod mm	Standoff distance
v_f mm•min^{-1}	Feed rate
P_{part} W	Jet power
E_{sp} J•mm^{-1}	Abrasive waterjet specific energy
c J•mm^{-3}	Material volume removed per unit energy
h mm	Sample thickness
w mm	Kerf width
T_R mm/mm	Taper ratio
$w_r(z)$ mm	Right side of the kerf profile
$w_l(z)$ mm	Left side of the kerf profile
$w_p(z)$ mm	Half kerf profile
$\overline{w}_p(z)$ mm	Average half kerf profile

✉ Massimiliano Annoni
massimiliano.annoni@polimi.it

1 Dipartimento di Meccanica, Politecnico di Milano, Via Giuseppe La Masa 1, 20156 Milan, Italy

2 Consorzio MUSP Macchine Utensili Sistemi di Produzione, via Callegari, 29122 Piacenza, Italy

1 Introduction

Abrasive waterjet cutting is a widespread process in many industrial sectors for cutting different classes of engineering materials [1–4] like metals [5–11], composites [12–15] and ceramic materials [16–19]. The abrasive waterjet cutting exploits a high energetic jet which mechanically removes the target material. The said process is classified as a cold mechanical material removal process that exhibits a series of advantages compared to the other non-conventional cutting process like low cutting forces, high flexibility intended as the capability of cutting different class of materials and the avoidance of any heat-affected zone. Other advantages include no limitations in the 2D-shape complexity and no mechanical contact with the workpiece, which makes it suitable for fragile and composite materials. The abrasive waterjet cutting head is represented in Fig. 1. Here, water flows through the primary orifice starting from a very high pressure, up to 600 MPa, resulting in a high-speed waterjet. Abrasive particles are fed with air into the mixing chamber; the resulting abrasive jet travels through the focusing tube, and momentum is transferred to the particles, which are consequently accelerated through the focusing tube [20, 21].

Waterjet velocity v_j (Eq. 3) can be derived from the theoretical velocity v_{th} (Eq. 1), that comes from the Bernoulli equation, considering water compressibility ψ (Eq. 2) and irreversibility c_v [21].

$$v_{th} = \sqrt{\frac{2p}{\rho}} \tag{1}$$

$$\psi = \sqrt{\frac{L}{p(1-n)}\left[\left(1+\frac{p}{L}\right)^{1-n}-1\right]} \tag{2}$$

(L = 300 MPa and n= 0.1368 [21, 22])

$$v_j = c_v \psi \sqrt{\frac{2p}{\rho}} \tag{3}$$

Water mass flow rate $\dot{m}_w$ (Eq. 4) is obtained from the water density ρ and water volume flow rate Q_w (Eq. 5), where S_n is the nominal cross-sectional area of the orifice, and c_d is the orifice discharge coefficient [2, 21]. The jet hydraulic power P_{hydr} is defined in Eq. 6.

$$\dot{m}_w = \rho Q_w \tag{4}$$

$$Q_w = c_d S_n \sqrt{\frac{2p}{\rho}} \tag{5}$$

$$P_{hydr} = \frac{1}{2}\dot{m}_w v_j^2 \tag{6}$$

During the mixing process, water transfers momentum to abrasive particles. The abrasive loading ratio r_d (Eq. 7) is introduced to explain the momentum transfer from the water to the abrasive particles. v_{abr}, Eq. 8, is the equilibrium velocity of the jet, when it exits from the focusing tube, under the hypothesis of no energy losses in the mixing process. Finally, Eq. 9 expresses the jet power P_{part}, which is the portion of the kinetic power of the abrasive waterjet that is useful for the material removal process, which means the kinetic power of the abrasive particles [20, 22, 23].

$$r_d = \frac{\dot{m}_a}{\dot{m}_w} \tag{7}$$

$$v_{abr} = \frac{v_j}{1+r_d} \tag{8}$$

$$P_{part} = \frac{1}{2}\dot{m}_a v_{abr}^2 \tag{9}$$

However, during the cutting process, the jet beam continuously loses its energy as it penetrates into the workpiece material, leading to an uneven kerf profile, which in turn

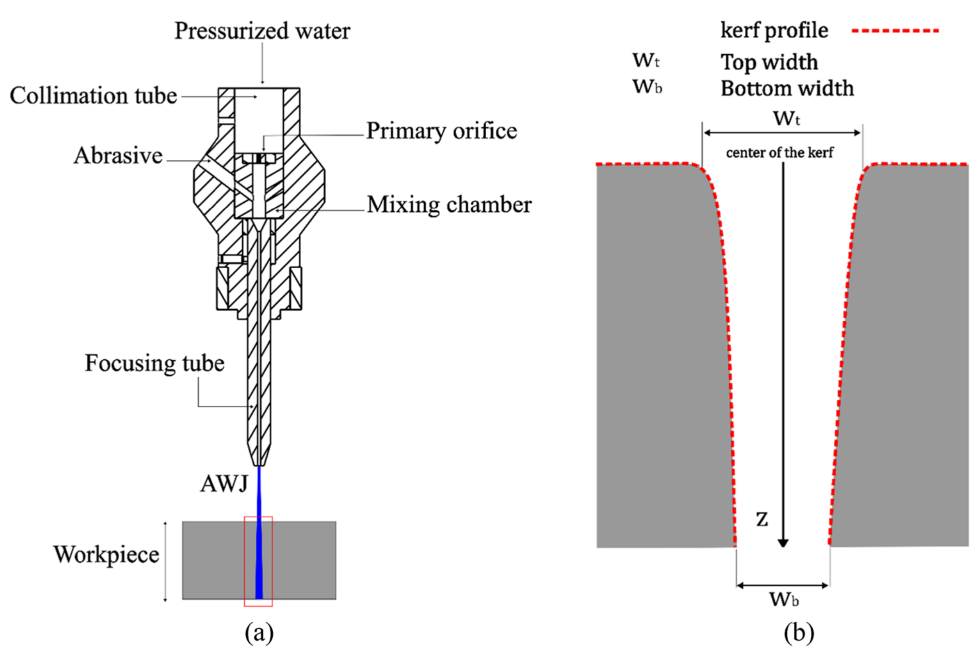

Fig. 1 **a** Abrasive waterjet cutting head. **b** Cross-sectional view of the kerf profile in abrasive waterjet cutting [22]

limits AWJ machining applications [12, 24, 25] since further machining processing may be needed to meet the required specifications. The resulting kerf geometry is usually characterized by the kerf taper ratio (Fig. 1b) that is related to the slope of the kerf walls. Arola and Ramulu [26] investigated the AWJ cutting of graphite-epoxy composites. They found that the kerf profile could be characterized by two different regions: the initial damage region (IDR) and the cutting region (CR). At shallow depth, the standoff distance was the most significant parameter on the profile, together with the feed rate. On the opposite, the water pressure, the abrasive mass flow rate and the feed rate were found to be the most significant in the CR. In [1], the effect of the feed rate on the kerf profile was investigated. A low traverse rate generated a negative taper, whereas high feed rates generated a linear profile with a positive taper. These results are consistent with [27], where the experiments were performed on acrylic plastic samples. The cut profile changed its shape according to the feed rate: from divergent to convergent. However, the effect of the other process parameters was not considered. An empirical correlation for the kerf profile shape was developed. In the IDR, the cut profile correlates well with the inverse of the cutting depth, showing a hyperbolic trend. In the CR, the profile was fitted with a second-order polynomial. The empirical model was able to capture the change in the kerf profile behaviour from a convergent to a divergent trend, according to the value of the feed rate. Wang et al. [24, 28] studied the influence of some process parameters on the kerf profile. Cutting experiments were performed on aluminium alloy 6061 T. Results showed that along with the feed rate and material's thickness, water pressure and abrasive flow rate had a significant effect on the shape of the kerf profile. Similarly, to [27], a full quadratic model was used to fit the kerf profile. The coefficients of the model were related to the natural logarithm of the ratio between the feed rate and the workpiece's thickness. However, there is no evidence for a clear correlation between them. Indeed, no results proving the significance of the correlation were reported. In [29], increasing water pressure and feed rate, the kerf taper was increased on nickel-based superalloy material. Kerf taper was found to be mostly affected by feed rate as well as by water pressure in a series of cutting experiments on multi-walled epoxy/carbon laminate [30]. The kinetic power of the abrasive waterjet particles (Eq. 10) represents a physical quantity that embodies the effect of some important process parameters in AWJ cutting. In literature, some studies showed that said quantity explains the AWJ cutting capability [31–33]. From Hashish's model [20], a strong relationship between the kerf profile and the kinetic power of the abrasive waterjet particles can be defined, as shown in Eq. 10.

$$h \cdot w \cdot v_{\mathrm{f}} = cP_{\mathrm{part}} \tag{10}$$

where h is the cutting depth, v_{f} is the jet feed rate, w is the kerf width, which is implicitly assumed to be the average of the kerf profile with respect to the cutting depth [21], and c represents the material volume removed per unit energy, that is, a property of the target material. The left-hand side of Eq. 10 represents the material removal rate. Finally, rearranging Eq. 11, it appears that the kerf width is proportional to the specific energy of the abrasive waterjet E_{sp} (from now on, it will be named as specific energy) that represents the theoretical mechanical energy of the abrasive particles per unit of cutting length.

$$hw \propto \frac{P_{\mathrm{part}}}{v_{\mathrm{f}}} = E_{\mathrm{sp}} = \frac{P_{\mathrm{part}}}{v_{\mathrm{f}}} = \frac{\dot{m}_{\mathrm{a}} \cdot v_{\mathrm{abr}}^2}{2v_{\mathrm{f}}} = \frac{\dot{m}_{\mathrm{a}} \cdot v_{\mathrm{j}}^2}{2v_{\mathrm{f}} \cdot \left(1 + r_{\mathrm{d}}\right)^2} = \frac{\dot{m}_{\mathrm{a}} \cdot c_{\mathrm{v}}^2 \cdot \psi^2 \cdot 2 \cdot p}{2 \cdot \rho \cdot v_{\mathrm{f}} \left(1 + \frac{\dot{m}_{\mathrm{a}}}{\dot{m}_{\mathrm{w}}}\right)^2} = \frac{\dot{m}_{\mathrm{a}} \cdot c_{\mathrm{v}}^2 \cdot \psi^2 \cdot p}{\rho \cdot v_{\mathrm{f}} \cdot \left(1 + \frac{\dot{m}_{\mathrm{a}}}{\rho \cdot Q_{\mathrm{w}}}\right)^2} = \frac{\dot{m}_{\mathrm{a}} \cdot c_{\mathrm{v}}^2 \cdot \psi^2 \cdot p}{\rho \cdot v_{\mathrm{f}} \cdot \left(1 + \frac{\dot{m}_{\mathrm{a}}}{\rho \cdot c_{\mathrm{d}} \cdot S_n \cdot \sqrt{\frac{2p}{\rho}}}\right)^2} \tag{11}$$

However, the literature review has shown that a systematically experimental study has not been conducted yet. The aim of the work was to experimentally investigate the influence of the AWJ-specific energy on the kerf profile in a series of AWJ cutting experiments on aluminium. Moreover, this paper would like to point out how the AWJ-specific energy is the most influential quantity on the kerf profile shape, more than each single process parameter. The kerf profile shape and kerf taper angle are investigated for this purpose.

2 Materials and methods

2.1 Sample preparation and experimental design

An aluminium 6082 plate (180 mm × 130 mm × 26 mm) was selected as the target workpiece for the experimental investigation. The experiments consisted of a series of AWJ cutting tests that were performed in one single pass on the aluminium plate once properly fixtured to minimize vibrations during the experiment. The experiment was designed and conducted according to the DOE (design of experiments) methodology. The following process parameters were considered as a variable in the experiments:

- Water pressure, p (MPa)
- Abrasive mass flow rate, $\dot{m}_{\mathrm{a}}$ (g•min^{-1})
- Feed rate, v_{f} (mm•min^{-1})

Table 1 Treatment combinations

Treatment combination	p (MPa)	$\dot{m}_a (g \cdot min^{-1})$	v_f ($mm \cdot min^{-1}$)	P_{part}(W)	E_{sp}(J•mm^{-1})	Set point (J•mm^{-1})	Quality reference
CTR	380	350	62	1574	1524	1500	Q6
EXP	303	300	43	1098	1532		
CTR	380	350	77	1574	1227	1200	Q5
EXP	300	300	53	1087	1230		
CTR	380	350	97	1574	973	950	Q4
EXP	196	200	31	500	967		

Table 2 Constant and control factors of the experimental plan

Constant factors	Values
Standoff distance, sod (mm)	3
Thickness, t (mm)	26
Primary orifice diameter, d_n (mm)	0.33
Focusing tube diameter, d_f (mm)	1.02
Focusing tube length, l_f (mm)	76.2
Impact angle, φ (°)	90
Type of abrasive	GMA Garnet
Abrasive mesh number	80
Control factors	Values
Treatment combination,T	CTR—EXP
Specific energy, E_{sp} (J•min^{-1})	950, 1200, 1500

Table 3 Experimental design matrix

Run order	$E_{sp} (J \cdot mm^{-1})$	T	p (MPa)	$\dot{m}_a (g \cdot min^{-1})$	v_f ($mm \cdot min^{-1}$)
1	950	CTR	380	350	97
2	950	CTR	380	350	97
3	1500	EXP	303	300	43
4	1500	CTR	380	350	62
5	1500	EXP	303	300	43
6	1200	EXP	300	300	53
7	1200	CTR	380	350	77
8	950	EXP	196	200	31
9	950	EXP	196	200	31
10	950	EXP	196	200	31
11	950	CTR	380	350	97
12	1500	CTR	380	350	62
13	950	EXP	196	200	31
14	1200	EXP	300	300	53
15	1500	EXP	303	300	43
16	1500	CTR	380	350	62
17	1200	EXP	300	300	53
18	1500	EXP	303	300	43
19	1200	CTR	380	350	77
20	950	CTR	380	350	97
21	1200	CTR	380	350	77
22	1200	EXP	300	300	53
23	1200	CTR	380	350	77
24	1500	CTR	380	350	63

The workpiece thickness was kept constant at 26 mm. Since the objective of the study was to investigate the effect of the AWJ-specific energy (E_{sp}) on the cutting quality, three levels of E_{sp} were tested. For each level, two different combinations of process parameters were selected. The first of the two (from now on called control, CTR) was determined from the built-in CAM software (ICam, © 2011 BIESSE S.p.A, Pesaro (Italy)) of the AWJ cutting apparatus, considering three levels of cutting quality: clean cut (Q3), good edge finish (Q4), excellent edge finish (Q5). Said levels were defined according to the ISO/TC 44 N 1770, which represent a standard industrial reference machining condition for waterjet cutting. The second combination (from now on called experimental, EXP) was found looking for a combination of process parameters that resulted in the same specific energy (Eq. 11), as reported in Table 1.

Afterwards, a multilevel factorial design was generated according to the statistical software MINITAB®. The experimental plan was replicated four times. The control factors of the experimental plan were the specific energy E_{sp} as well as the type of treatment combination, T (CTR/EXP, i.e., a categorical factor). Both factors, with their levels, are reported in Table 2, along with constant factors of the experimental design.

The experimental design matrix in the randomized run order is reported in Table 3.

The experimental plan was carried out on a 5-axis CNC abrasive waterjet machine (PRIMUS 322, Intermac BIESSE, Pesaro (Italy)) (Fig. 2), with a double-effect high-pressure intensifier pump (Ecotron 40.37, BFT GmbH, Hönigsberg, Austria).

The technical specifications of the pressure intensifier were 37 kW of power requirement, the operating maximum pressure was 380 MPa and the maximum water flow rate was

Fig. 2 AWJ cutting apparatus

3.5 L•min^{-1}. A pressure gauge was mounted at the pressure intensifier outlet to measure water pressure in every experimental run. Abrasive mass flow rate was regulated by an abrasive dosing system. The maximum abrasive mass flow was 350 g•min^{-1}. Australian GMA Garnet, mesh 80, was used as abrasive powder.

2.2 Kerf profile measurement and data analysis

The geometric characteristic of each cutting kerf was carried out using the Quick Vision Pro system, manufactured by Mitutoyo, Sakado, Japan. The Quick Vision Pro system is a precision measurement tool known for its accuracy and reliability, making it well suited for the precise assessment of the kerf profiles in abrasive waterjet (AWJ) cutting. It offers advanced capabilities for dimensional measurements, ensuring the collection of high-quality data. The acquired images were processed in a Matlab (Mathworks Inc, Massachusetts, USA) software. Image analysis was applied to extract the kerf profile according to a method that was developed on purpose. For each experimental run, a grayscale image of the cutting kerf was acquired (Fig. 3a) and binarized (Fig. 3b) to

Fig. 3 Sequence of the image processing method. The experimental run was performed at p = 380 MPa, v_f = 97 mm · min^{-1} and $\dot{m}_a$ = 350 g•min^{-1}

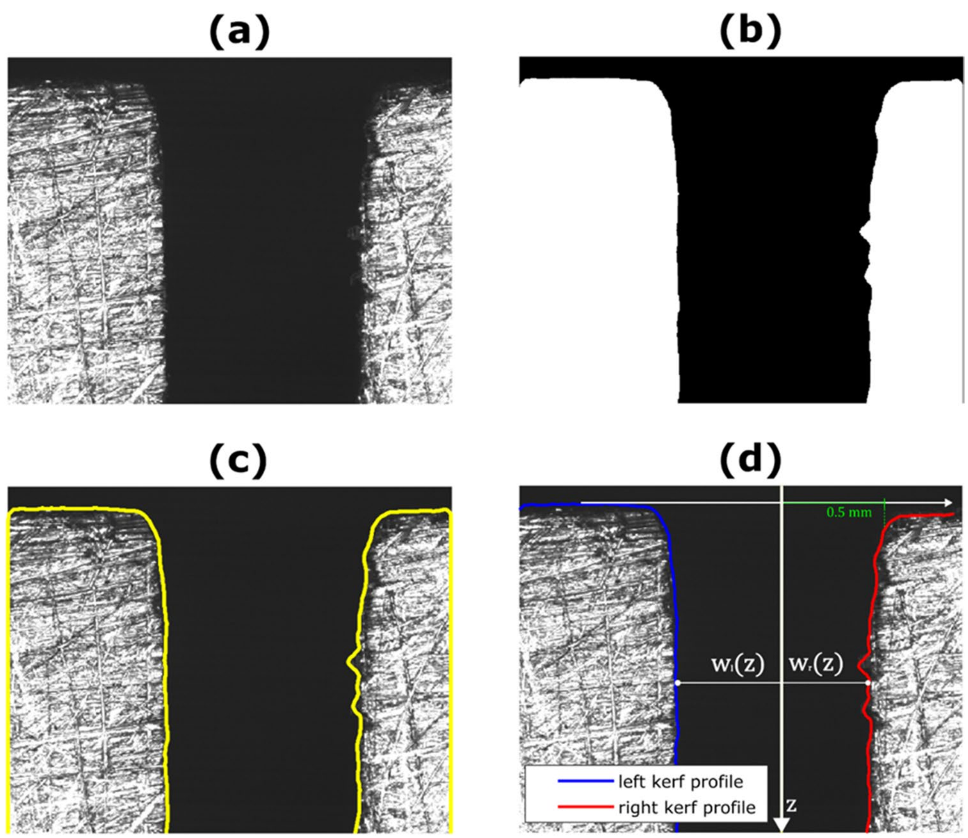

highlight the physical boundary of the kerf (Fig. 3c). Finally, the set of both left and right kerf boundary coordinates was extracted from the processed image (Fig. 3d).

Data analysis was conducted according to the following steps.

1. Kerf profile modelling

Each side of the cutting kerf may be modelled as a function of the depth. These quantities represent the distance between the kerf wall and the centre of the kerf profile, i.e., $w_r(z)$ and $w_l(z)$ (Fig. 3d). However, pre-experimental results showed that the two side of the cutting kerf could be considered plausibly symmetric. For this reason, for the sake of simplicity and conciseness, the half kerf profile, $w_p(z) = f(z;\beta)$, was introduced (Eq. 12), where z is the spatial coordinate with respect the axis of the cutting kerf (Fig. 3d), while β is the vector of the unknown parameters. $w_p(z)$ represents the half profile of the kerf width. The orientation of the width axis is arbitrary, and it was set positive toward the right side of the kerf profile; for this reason, it was taken as the absolute of $w_l(z)$ in Eq. 12.

The spatial profile in the initial damage region IDR was modelled as an exponential term, which rapidly drops to zero where the cutting region CR starts, while a linear profile was assumed to model the cutting region. The equation of the model contains four unknown coefficients, as reported in Eq. 12, where ε represents the error term.

$$w_p(z) = \frac{w_r(z) + |w_l(z)|}{2} = a + be^{-cz} + dz + \varepsilon \quad (12)$$

Non-linear regression analysis, based on Levenberg-Marquardt algorithm (MLA), was exploited to fit experimental data to the model and find the unknown coefficients. It is important to consider that the combinations of control factors produced a convergent kerf geometry for all experimental conditions.

2. Kerf geometry characterization

For each experimental run, the top width w_t was measured at 1 mm below the upper surface of the sample, while the bottom width (w_b) was measured at 2 mm over the lower surface of the sample (Fig. 1b). The taper ratio T_R was calculated as in Eq. 13 [1].

$$T_R = \frac{w_t}{w_b} \quad (13)$$

3. Statistical analysis

Experimental data were analyzed, and the ANOVA was performed to formally test the significance of the control factors on the taper ratio.

3 Results

3.1 Empirical modelling of the kerf profile

The estimated coefficients of the model (Eq. 12) are reported in Table 4 for each experimental run.

For the sake of clear and concise representation, the average half kerf profile $\overline{w}_p(z)$, across different levels of the abrasive waterjet specific energy and for each treatment type (CTR, EXP), are reported in Fig. 4. For each subplot, the solid lines represent experimental data: the blue line indicates the CTR treatment type, while the red line indicates the EXP treatment type. Dashed lines represent the fitted data of the average half kerf profile $\overline{w}_p(z)$. Said quantity was modelled assuming the same mathematical structure defined in Eq. 12. Non-linear regression analysis, based on the Levenberg-Marquardt algorithm (MLA), was used to fit experimental data to the model and find the unknown coefficients. The trends of the kerf profiles appear to be convergent with respect to the depth of cut for each combination of specific energy and treatment type. The type of treatment seems to be less influential on the slope of the kerf profile than specific energy. The initial damage region seems not to be influenced by the level of the specific energy E_{sp}: both the curvature of the round edge and the width do not show any evident trend. However, in the cutting region, the effect of the specific energy on the slope of the kerf profile seems to be more evident.

In support of this statement, the behaviour of the slope coefficients of the kerf profile, i.e., the coefficients d of the model (Eq. 12) obtained for the different experimental runs, was evaluated with respect to the control factors (Fig. 5).

The coefficient d (Eq. 12), which gives the inclination of the kerf in the cutting region, varied with the specific energy: the higher the specific energy, the lower the slope of the cutting kerf (consider the modulus of d). The results reveal a significant influence of the specific energy of the jet on the slope of the cutting kerf, as indicated by the coefficients of the model. Notably, for each level of specific energy, the range of variability under the type of treatment combination appears to be comparable. The difference in slope of the profiles is less pronounced when going from 1200 to 1500 J/mm compared to the difference between 950 and 1200 J/mm. The taper ratio was calculated for each experimental run, and the effect of the

Table 4 Kerf profile model coefficients for each experimental run

Run order	E_{sp}(J/mm)	T	a	b	c	d	R^2_{adj}
1	950	CTR	0.606492	0.2868	20.1592	−0.0063	0.9628
2	950	CTR	0.581052	0.5084	39.4823	−0.0072	0.9552
3	1500	EXP	0.604543	0.3225	10.3073	−0.0081	0.9603
4	1500	CTR	0.600599	0.2268	5.2286	−0.0082	0.9613
5	1500	EXP	0.599569	0.2596	8.3289	−0.0065	0.9234
6	1200	EXP	0.604153	0.2620	8.5714	−0.0056	0.9309
7	1200	CTR	0.58801	0.3195	9.0388	−0.0061	0.9323
8	950	EXP	0.571846	0.2221	6.0607	−0.0067	0.9784
9	950	EXP	0.556671	0.2677	5.9408	−0.0065	0.9522
10	950	EXP	0.56038	0.3456	13.8416	−0.0053	0.9411
11	950	CTR	0.594356	0.1773	2.7903	−0.0070	0.9607
12	1500	CTR	0.591572	0.3264	7.9326	−0.0066	0.9553
13	950	EXP	0.573337	0.1892	3.3117	−0.0057	0.9307
14	1200	EXP	0.609091	0.1864	3.3403	−0.0057	0.9451
15	1500	EXP	0.611434	0.3049	8.3818	−0.0060	0.9505
16	1500	CTR	0.610249	0.3987	11.3910	−0.0071	0.9412
17	1200	EXP	0.601528	0.2173	4.0204	−0.0054	0.9411
18	1500	EXP	0.603255	0.3342	8.8469	−0.0053	0.9032
19	1200	CTR	0.61807	0.2799	7.1272	−0.0060	0.9502
20	950	CTR	0.606496	0.3455	11.1929	−0.0065	0.9598
21	1200	CTR	0.600788	0.2036	3.5988	−0.0047	0.9537
22	1200	EXP	0.611791	0.2339	5.5685	−0.0048	0.9592
23	1200	CTR	0.597415	0.2281	5.2485	−0.0051	0.9514
24	1500	CTR	0.618925	0.2985	8.5243	−0.0062	0.9477

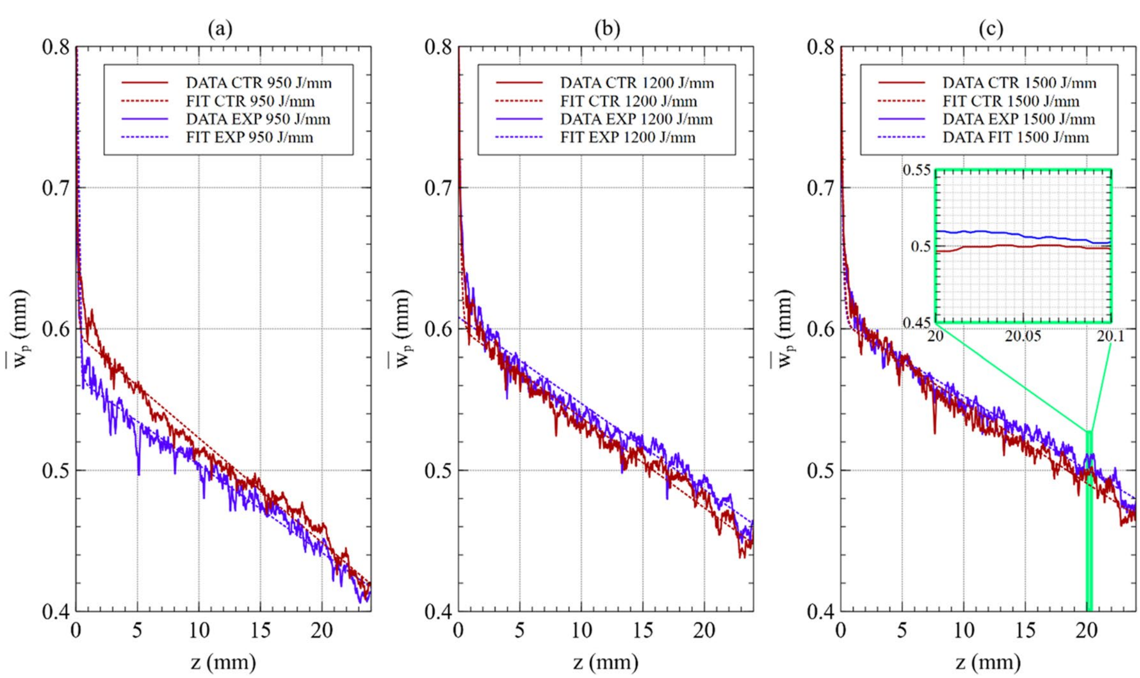

Fig. 4 Average half kerf profiles at different specific energy values for different type of treatment combination: **a** 950 J/mm, **b** 1200 J/mm, **c** 1500 J/mm. Solid lines represent experimental data. Dashed lines represent fitted data

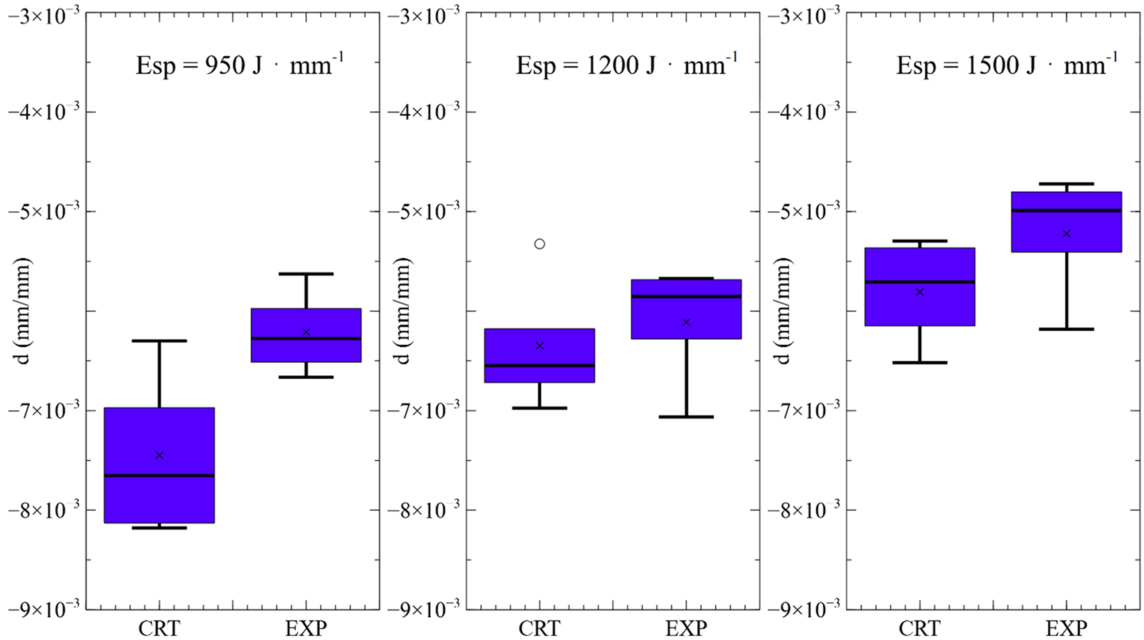

Fig. 5 Slope coefficients d across different levels of specific energy and treatment combinations. For each level of specific energy, the boxplot under each type of treatment combination was obtained considering the four replicates defined into the design matrix of the experimental plan (Table 3)

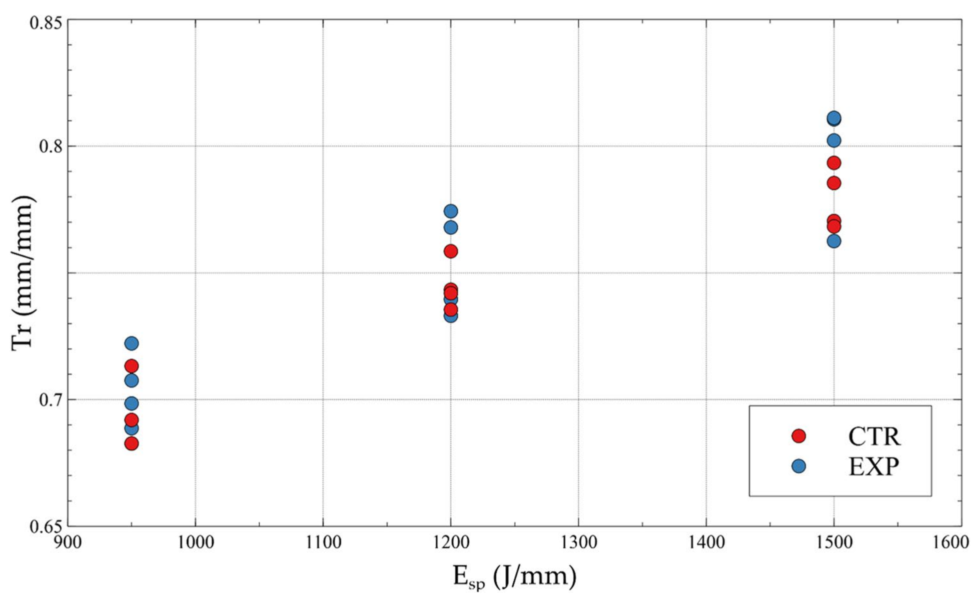

Fig. 6 Scatterplot of the taper ratio at different levels of the specific energy

specific energy E_{sp} and the effect of the treatment combinations T are graphically represented in Fig. 6.

A summary of the minimum, maximum and average values of the taper ratio is reported in Table 5.

Results show that the variability of the taper ratio across the different levels of the specific energy seems to be comparable among the two types of treatment combination (CTR, EXP). The ANOVA was conducted to test for the significance of the control factors (Table 6). The specific energy was found to be the most significant factor (p-value $= 3.06 \cdot 10^{-6}$) while the treatment combination factor was found to be slightly significant (p-value $= 0.0691$).

Table 5 Descriptive statistics of the taper ratio

Set point	T	Average (mm/mm)	Min. (mm/mm)	Max. (mm/mm)
950	CTR	0.6926	0.6826	0.7132
950	EXP	0.7042	0.6887	0.7132
1200	CTR	0.7448	0.7355	0.7222
1200	EXP	0.7537	0.7331	0.7585
1500	CTR	0.7794	0.7683	0.7934
1500	EXP	0.7966	0.7626	0.8111

Table 6 ANOVA table for taper ratio T_R

Source	DF	Sum sq	Mean sq	F-value	p-value
E_{sp}	1	0.03176	0.03176	123.052	$3.06\ 10^{-6}$
T	1	0.00095	0.00095	4.2697	0.0691
Residuals	21	0.00542	0.00026		

and predict the geometry of the kerf profile. More precisely, combinations of process parameters resulting in the same specific energy allow, on average, to obtain the same cutting quality level, expressed as a taper ratio. Therefore, the specific energy could be considered as an aggregate physical quantity instead of using individual process parameters to achieve a prescribed level of cutting quality.

Nevertheless, it is essential to acknowledge certain limitations of this study. While the experimental investigation and modelling provide valuable insights, the research was conducted specifically on aluminium 6082. Thus, the generalizability of the findings to other materials and conditions should be further explored. Additionally, the study focused on the spatial kerf profile and taper angle, neglecting other important aspects of cutting quality, such as surface roughness or material integrity. Future research should aim to address these limitations.

The correlation between the kerf taper and the specific energy can be effectively represented by relating the jet power to the feed rate. In Fig. 7, the empirical relationship between these two variables is represented. It is important to note that each level of cutting quality corresponds to a specific energy level. Hence, within the experimental range, any pair of values (P_{part}, v_f) that satisfies the equation $\frac{P_{part}}{v_f} = E_{sp} =$ cost represents a combination of cutting conditions that yield the same average taper ratio. To provide a more formal representation of this result and its practical implications, a graphical representation can be employed. By plotting the iso-specific energy lines in the $P_{part} - v_f$ plane, each circle on the graph corresponds to a specific combination of (P_{part}, v_f) as determined by the values

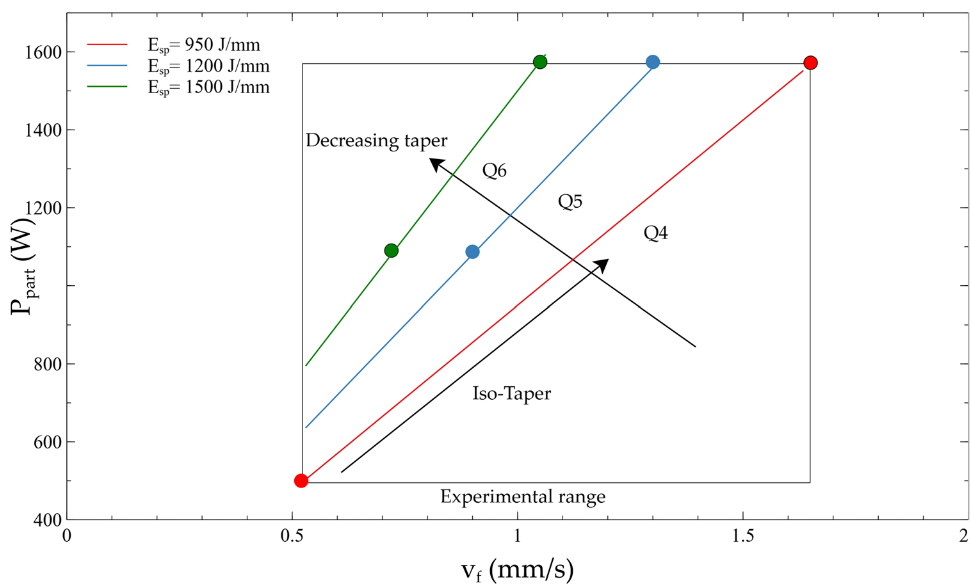

Fig. 7 Iso-specific energy lines into the $P_{part} - v_f$ plane: correlation between the abrasive waterjet specific energy and taper ratio. For each iso-specific energy line, each circle represents a combination of ($P_{part} - v_f$) according to Table 1

4 Discussion

In agreement to literature [16, 29, 30], the results of the present study show how all the control factors of the experiment contribute significantly to the kerf profile. From this perspective, the study extends and generalize those of Wang [28], whose limitation results in having considered only the effect of the feed rate on the shape of the kerf profile. Indeed, both abrasive mass flow rate and water pressure were found to be significant, together with the feed rate.

The results of the present work show that there is a region of abrasive waterjet process parameters where the specific energy delivers the same information to describe presented in Table 1. The iso-specific energy lines help visualize the relationship between the jet power, feed rate and taper ratio. By selecting a point on any given iso-specific energy line, into the experimental range, the corresponding cutting conditions (i.e., water pressure and abrasive mass flow rate, Eq. 11) that result in a consistent taper ratio can be determined.

5 Conclusions

In this paper, a comprehensive investigation into the effect of the abrasive waterjet specific energy on the spatial kerf profile during abrasive waterjet cutting was conducted. Through a series of cutting experiments on aluminium 6082, the kerf profile exhibited a linear trend with respect to the cutting depth, with its slope being influenced by the level of the abrasive waterjet specific energy. Specifically, higher specific energy levels resulted in a lower taper ratio of the cutting kerf.

To systematically analyze and characterize the kerf spatial profile, an empirical model using nonlinear regression analysis was developed. The model demonstrated a good agreement with the experimental data (R^2_{adj}> 0.95) and effectively reproduced the behaviour of the kerf profile within the cutting region. Notably, the coefficients of the model were highly correlated with the abrasive waterjet specific energy, indicating their significance in predicting and controlling the kerf profile. Furthermore, results showed that combinations of process parameters resulting in the same abrasive waterjet specific energy consistently produced similar kerf profiles on average. As a consequence, results proved a connection between the Q-levels, which are defined according to the surface quality of the kerf walls and their inclination. This observation highlights the potential of utilizing the abrasive waterjet specific energy as a comprehensive physical quantity to achieve a desired kerf profile. A graphical representation of the taper ratio into the $P_{part} - v_f$ plane was introduced. Said representation may offer practical utility to the technology end-users to quickly identify the appropriate combination of jet power and feed rate to achieve a desired taper ratio without the need for extensive experimentation. It may provide a valuable tool for process optimization and control, allowing for efficient and accurate adjustments to achieve the desired kerf taper. Once the cutting quality in terms of taper ratio, i.e., Q, has been established, one may proceed along the corresponding iso-taper line to identify the optimal productivity conditions. Finally, the experimental results strengthened the importance of the specific energy as the quantity that contributes to the quality of the cutting process. Therefore, monitoring this quantity by using the methods shown by [31–33] could enable an in-line control of the process as well as its quality. As a future step, the study could be integrated with an experimental investigation of the specific energy as a potential means of characterizing the transition between convergent and divergent trends in the kerf profile, with the potential objective of minimizing taper inclination and obtaining vertical kerf walls. By optimizing the specific energy, it may be possible to precisely control and enhance the cutting quality. In conclusion, this study provides valuable insights into the influence of the abrasive waterjet specific energy on the spatial kerf profile in abrasive waterjet cutting. The identified correlations offer a valuable framework for understanding and predicting the kerf profile geometry. The findings may contribute to advancing the understanding of the abrasive waterjet cutting quality and an alternative way for optimizing the abrasive waterjet cutting process, with various industrial applications.

Author contribution F.P conceived the conceptualization and the methodology, designed and performed the experiments and wrote the paper. M.A conceived the research and supervised and reviewed the manuscript. M.M performed the proofreading of the paper.

Funding This research received no external funding.

Data availability The data that support the findings of this study are available on request from the corresponding author.

Declarations

Competing interests The authors no competing interests.

References

1. Momber AW, Kovacevic R (1998) Principles of abrasive water jet machining. Springer, London
2. Monno M, Annoni M, Ravasio C (2007) Water jet, a flexible technology. Polipress, Milano
3. Liu X, Liang Z, Wen G, Yuan X (2019) Waterjet machining and research developments: a review. Int J Adv Manuf Technol 102(5–8):1257–1335. https://doi.org/10.1007/s00170-018-3094-3
4. Wang J (2003) The effect of jet impinging angle on the cutting performance in AWJ machining of alumina ceramics. Key Eng Mater 238–239:117–122
5. Llanto JM, Tolouei-Rad M, Vafadar A, Aamir M (2021) Recent progress trend on abrasive waterjet cutting of metallic materials: a review. Appl Sci 11(8):3344. https://doi.org/10.3390/app11083344
6. Li H, Wang J (2015) An experimental study of abrasive waterjet machining of Ti-6Al-4V. Int J Adv Manuf Technol 81(1–4):361–369. https://doi.org/10.1007/s00170-015-7245-5
7. Ay M, Çaydaş U, Hasçalik A (2010) Effect of traverse speed on abrasive waterjet machining of age hardened Inconel 718 nickel-based superalloy. Mater Manuf Process 25(10):1160–1165. https://doi.org/10.1080/10426914.2010.502953
8. Llanto JM, Vafadar A, Aamir M, Tolouei-Rad M (2021) Analysis and optimization of process parameters in abrasive waterjet contour cutting of AISI 304L. Metals 11(9):1362. https://doi.org/10.3390/met11091362

9. Rokosz K (2022) Surface engineering of metals and alloys. Metals 12(4):542. https://doi.org/10.3390/met12040542
10. Llanto JM, Tolouei-Rad M, Vafadar A, Aamir M (2021) Impacts of traverse speed and material thickness on abrasive waterjet contour cutting of austenitic stainless steel AISI 304L. Appl Sci 11(11):4925. https://doi.org/10.3390/app11114925
11. Perec A (2018) Experimental research into alternative abrasive material for the abrasive water-jet cutting of titanium. Int J Adv Manuf Technol 97(1–4):1529–1540. https://doi.org/10.1007/s00170-018-1957-2
12 Ishfaq K, Ahmad Mufti N, Ahmed N, Pervaiz S (2019) Abrasive waterjet cutting of cladded material: kerf taper and MRR analysis. Mater Manuf Process 34(5):544–553. https://doi.org/10.1080/10426914.2018.1544710
13. Unde PD, Gayakwad MD, Patil NG, Pawade RS, Thakur DG, Brahmankar PK (2015) Experimental investigations into abrasive waterjet machining of carbon fiber reinforced plastic. J Compos 2015:1–9. https://doi.org/10.1155/2015/971596
14. Doreswamy D, Shivamurthy B, Anjaiah D, Sharma NY (2015) An investigation of abrasive water jet machining on graphite/glass/epoxy composite. Int J Manuf Eng 2015:1–11. https://doi.org/10.1155/2015/627218
15. Sambruno A, Bañon F, Salguero J, Simonet B, Batista M (2019) Kerf taper defect minimization based on abrasive waterjet machining of low thickness thermoplastic carbon fiber composites C/TPU. Materials 12(24):4192. https://doi.org/10.3390/ma12244192
16. Srinivasu DS, Axinte DA, Shipway PH, Folkes J (2009) Influence of kinematic operating parameters on kerf geometry in abrasive waterjet machining of silicon carbide ceramics. Int J Mach Tools Manuf 49(14):1077–1088. https://doi.org/10.1016/j.ijmachtools.2009.07.007
17. Tiwari T et al (2018) Parametric investigation on abrasive waterjet machining of alumina ceramic using response surface methodology. IOP Conf Ser: Mater Sci Eng 377:012005. https://doi.org/10.1088/1757-899X/377/1/012005
18. Dugar J, Ikram A, Pušavec F (2021) Comparative characterization of different cutting strategies for the sintered ZnO electroceramics. Appl Sci 11(20):9410. https://doi.org/10.3390/app11209410
19. Hamatani G, Ramulu M (1990) Machinability of high temperature composites by abrasive waterjet. J Eng Mater Technol 112(4):381–386. https://doi.org/10.1115/1.2903346
20. Hashish M (2014) Kinetic power density in waterjet cutting. In: Proceeding of BHR Group - 22nd International Conference on Water Jetting
21. Hashish M (1989) Pressure effects in abrasive-waterjet (AWJ) machining. J Eng Mater Technol 111(3):221–228. https://doi.org/10.1115/1.3226458
22. Perotti F, Annoni M, Calcante A, Monno M, Mussi V, Oberti R (2021) Experimental study of abrasive waterjet cutting for managing residues in no-tillage techniques. Agriculture 11(5):392. https://doi.org/10.3390/agriculture11050392
23. Perotti F, Mossini E, Macerata E, Annoni M, Monno M (2023) Applicability of abrasive waterjet cutting to irradiated graphite decommissioning. Nucl Eng Technol 55(7):2356–2365. https://doi.org/10.1016/j.net.2023.03.026
24. Wang S, Zhang S, Wu Y, Yang F (2017) Exploring kerf cut by abrasive waterjet. Int J Adv Manuf Technol 93(5–8):2013–2020. https://doi.org/10.1007/s00170-017-0467-y
25. Wang S, Hu D, Yang F, Lin P (2022) Research on kerf error of aluminum alloy 6061–T6 cut by abrasive water jet. Int J Adv Manuf Technol 118(7–8):2513–2521. https://doi.org/10.1007/s00170-021-08056-5
26. Arola D, Ramulu M (1996) A study of kerf characteristics in abrasive waterjet machining of graphite/epoxy composite. J Eng Mater Technol 118(2):256–265. https://doi.org/10.1115/1.2804897
27. Ma C, Deam RT (2006) A correlation for predicting the kerf profile from abrasive water jet cutting. Exp Thermal Fluid Sci 30(4):337–343. https://doi.org/10.1016/j.expthermflusci.2005.08.003
28. Wang S, Zhang S, Wu Y, Yang F (2017) A key parameter to characterize the kerf profile error generated by abrasive water-jet. Int J Adv Manuf Technol 90(5–8):1265–1275. https://doi.org/10.1007/s00170-016-9402-x
29. Uthayakumar M, Khan MA, Kumaran ST, Slota A, Zajac J (2016) Machinability of nickel-based superalloy by abrasive water jet machining. Mater Manuf Process 31(13):1733–1739. https://doi.org/10.1080/10426914.2015.1103859
30. Thakur RK, Singh KK (2020) Experimental investigation and optimization of abrasive water jet machining parameter on multi-walled carbon nanotube doped epoxy/carbon laminate. Measurement 164:108093. https://doi.org/10.1016/j.measurement.2020.108093
31. Copertaro E, Perotti F, Castellini P, Chiariotti P, Martarelli M, Annoni M (2020) Focusing tube operational vibration as a means for monitoring the abrasive waterjet cutting capability. J Manuf Process 59:1–10. https://doi.org/10.1016/j.jmapro.2020.09.040
32. Copertaro E, Perotti F, Annoni M (2021) Operational vibration of a waterjet focuser as means for monitoring its wear progression. Int J Adv Manuf Technol 116(5–6):1937–1949. https://doi.org/10.1007/s00170-021-07534-0
33. Copertaro E, Annoni M (2022) Airborne acoustic emission of an abrasive waterjet cutting system as means for monitoring the jet cutting capability. Int J Adv Manuf Technol 123(7–8):2655–2667. https://doi.org/10.1007/s00170-022-10317-w